

Article

Microwave-Assisted Hydrothermal Synthesis of Space Fillers to Enhance Volumetric Energy Density of NMC811 Cathode Material for Li-Ion Batteries

Irina Skvortsova, Aleksandra A. Savina , Elena D. Orlova, Vladislav S. Gorshkov  and Artem M. Abakumov * 

Center for Energy Science and Technology, Skolkovo Institute of Science and Technology, Nobel str. 3, 121205 Moscow, Russia; irina.skvortsova@skoltech.ru (I.S.); a.savina@skoltech.ru (A.A.S.); elena.orlova2@skoltech.ru (E.D.O.); v.gorshkov@skoltech.ru (V.S.G.)

* Correspondence: a.abakumov@skoltech.ru

Abstract: Ni-rich layered transition metal (TM) oxides are considered to be the most promising cathode materials for lithium-ion batteries because of their high electrochemical capacity, high Li^+ ion (de)intercalation potential, and low cobalt content. However, such materials possess several drawbacks including relatively low volumetric energy density caused by insufficient values of tap density. Herein, we demonstrate an exceptionally rapid and energy-saving synthesis of the mixed hydroxide precursor for the $\text{LiNi}_{0.8}\text{Mn}_{0.1}\text{Co}_{0.1}\text{O}_2$ (NMC811) positive electrode (cathode) material through a microwave-assisted hydrothermal technique. The obtained material further serves as a space-filler to fill the voids between spherical agglomerates in the cathode powder prepared via a conventional co-precipitation technique boosting the tap density of the resulting mixed NMC811 by 30% up to 2.9 g/cm^3 . Owing to increased tap density, the volumetric energy density of the composite cathode exceeds 2100 mWh/cm^3 vs. 1690 mWh/cm^3 for co-precipitated samples. The crystal structure of the obtained materials was scrutinized by powder X-ray diffraction and high angle annular dark-field scanning transmission electron microscopy (HAADF-STEM); the cation composition and homogeneity of TM spatial distribution were investigated using energy-dispersive X-ray spectroscopy in a STEM mode (STEM-EDX). Well-crystallized NMC811 with a relatively low degree of anti-site disorder and homogeneous TM distribution in a combination with the co-precipitated material delivers a reversible discharge capacity as high as $\sim 200 \text{ mAh/g}$ at 0.1C current density and capacity retention of 78% after 300 charge/discharge cycles (current density 1C) within the voltage region of $2.7\text{--}4.3 \text{ V}$ vs. Li/Li^+ .



Citation: Skvortsova, I.; Savina, A.A.; Orlova, E.D.; Gorshkov, V.S.; Abakumov, A.M.

Microwave-Assisted Hydrothermal Synthesis of Space Fillers to Enhance Volumetric Energy Density of NMC811 Cathode Material for Li-Ion Batteries. *Batteries* **2022**, *8*, 67. <https://doi.org/10.3390/batteries8070067>

Academic Editor: Yu-Sheng Su

Received: 11 June 2022

Accepted: 4 July 2022

Published: 6 July 2022

Publisher's Note: MDPI stays neutral with regard to jurisdictional claims in published maps and institutional affiliations.



Copyright: © 2022 by the authors. Licensee MDPI, Basel, Switzerland. This article is an open access article distributed under the terms and conditions of the Creative Commons Attribution (CC BY) license (<https://creativecommons.org/licenses/by/4.0/>).

1. Introduction

Among the currently used positive electrode (cathode) materials for lithium-ion batteries (LIBs), the layered oxides $\text{LiNi}_x\text{Mn}_y\text{Co}_z\text{O}_2$ ($x + y + z = 1$, also designated as NMCXYZ, where X:Y:Z is the molar ratio of Ni, Mn, and Co) offer superior electrochemical capacities compared to conventional LiCoO_2 ($\sim 140 \text{ mAh/g}$), LiMn_2O_4 ($\sim 120 \text{ mAh/g}$) and LiFePO_4 ($\sim 160 \text{ mAh/g}$). NMCs with high nickel content ($x > 0.6$, Ni-rich NMCs) provide a high specific capacity of up to 220 mAh/g at a high working voltage ($\sim 3.6\text{--}3.8 \text{ V}$), being commonly regarded as the most promising for automotive LIBs [1,2]. Besides gravimetric energy density, the volumetric energy density of Ni-rich NMCs is another important parameter for practical applications, but here Ni-rich NMCs demonstrate certain deficiencies because of relatively low values of tap density. For instance, NMC811 cathode materials obtained via a co-precipitation method as the most preferred method for commercial production of NMC, consist of spherical secondary particles. Such polycrystalline materials are characterized by a limited tap density of $2.20\text{--}2.45 \text{ g/cm}^3$, corresponding to a volumetric energy

density of 1700 mWh/cm³, which is relatively low for providing suitable mileage of electric vehicles while keeping acceptable size and mass of the battery [3,4]. Several attempts have been incorporated to achieve enhanced tap density values by variation of co-precipitation synthesis conditions, including pH [5], temperature [6], and the molar ratio of TM and complexing agent [6]. Apart from this, the shape [7] and sizes of the secondary particles [8] were tuned to obtain Ni-rich NMCs with proper tap density. Despite some progress, the ultimate values of tap density are already attained.

The most facile way to increase the tap density of Ni-rich NMCs is to fill the voids between closely-packed spherical secondary particles. Such a method was suggested in Ref. [9] and is considered to be commercially prospective. However, obtaining two or three fractions of materials with different sizes by co-precipitation technique makes the cathode materials fabrication time-consuming and, therefore, more expensive. To enhance the energy- and resource efficiency of synthesis, a microwave-assisted hydrothermal route for preparing the Ni-rich hydroxide precursors is an attractive approach to produce a submicron-sized NMC fraction. Unlike the co-precipitation method, the microwave-assisted hydrothermal route does not require the continuous control of such synthesis parameters as pH, stirring rate, feeding rate of reagents, etc. This, in turn, relaxes the requirements of the equipment and reduces the materials production costs. Moreover, microwave radiation, transferring energy directly to the reacting species, can shorten the synthesis procedure from dozens of hours to several minutes, making this method one of the most energy- and cost-effective [10–13].

Herein, we report a strategy to prepare the mixed hydroxide $\text{Ni}_{0.8}\text{Mn}_{0.1}\text{Co}_{0.1}(\text{OH})_2$ precursor via the microwave-assisted hydrothermal method based on inexpensive and readily available raw reagents. Furthermore, we demonstrate the utilization of the prepared NMC811 cathode material as a space filler for ~30% improvement of volumetric energy density by properly mixing it with the material obtained through the conventional co-precipitation route.

2. Results and Discussion

A series of mixed hydroxide $\text{Ni}_{0.8}\text{Mn}_{0.1}\text{Co}_{0.1}(\text{OH})_2$ precursors was prepared via a microwave-assisted hydrothermal synthesis according to the scheme presented in Figure 1.

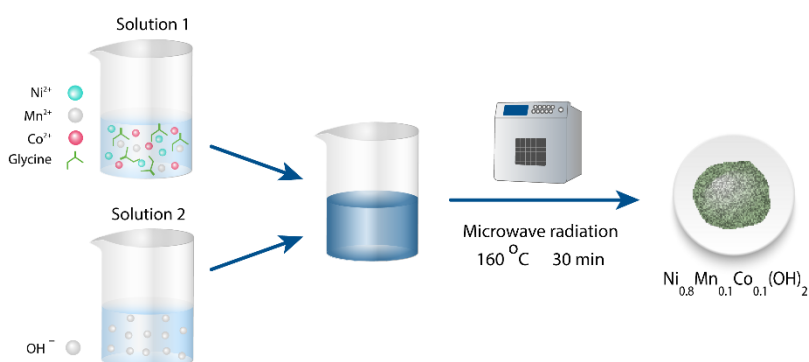


Figure 1. Scheme of the mixed hydroxide precursor $\text{Ni}_{0.8}\text{Mn}_{0.1}\text{Co}_{0.1}(\text{OH})_2$ synthesis via a microwave-assisted hydrothermal route.

An aqueous solution of transition metal (TM) sulfates taken in an appropriate molar ratio and glycine as a complexing agent was mixed with a solution of sodium hydroxide, transferred to a Teflon reactor for microwave-assisted hydrothermal synthesis, and treated at $160\text{ }^\circ\text{C}$ for 15–60 min to obtain the mixed hydroxide precursor (see details in Materials and Methods). The role of glycine as a complexing agent has been demonstrated before in hydrothermal synthesis of $\beta\text{-Ni}(\text{OH})_2$, where it prevents immediate precipitation of nickel(II) hydroxide when sodium hydroxide solution is added into the reaction mixture [14–16]. However, in contrast to the precipitation of $\beta\text{-Ni}(\text{OH})_2$, the synthesis of the mixed hydroxide $\text{Ni}_{0.8}\text{Mn}_{0.1}\text{Co}_{0.1}(\text{OH})_2$ precursor with homogeneous TM distribution

and desired composition requires the simultaneous formation of stable Ni(II), Mn(II) and Co(II) complexes with glycine in the initial solution. Therefore, the influence of TM:Gly and TM:NaOH molar ratios on the cation composition and homogeneity of TM spatial distribution in the hydroxide precursors obtained through the microwave-assisted hydrothermal technique was investigated. According to STEM-EDX, the TM:Gly ratio of 1:13.35 and TM:NaOH ratio of 1:25 were found to be optimal, providing a precipitated product with stoichiometry close to NMC811 with homogeneous TM distribution. Decreasing the TM:Gly molar ratio to 1:12.35 results in Mn and Co segregation (Figure S1), whereas further increase of the glycine content (TM:Gly > 1:13.35) is limited by its solubility in water (25 g/100 mL at 25 °C) [17]. The excessive amount of NaOH (TM:NaOH = 1:25) is required not only for co-precipitation of the hydroxide precursor but also for sustaining alkali conditions (pH > 11) [14]. Lower TM:NaOH molar ratio (1:20) results in a formation of $\text{Ni}_{0.8}\text{Mn}_{0.1}\text{Co}_{0.1}(\text{OH})_2$ consisting of small (150–200 nm) poorly agglomerated primary particles (Figure S2), while the deep blue color of the supernatant manifests incomplete precipitation. Since the TM:Gly and TM:NaOH molar ratios were optimized, the influence of treatment time on the precursor morphology and electrochemical performance of the final cathode material was investigated. The obtained precursors are labeled as MW_15m, MW_30m and MW_60m, where the numbers indicate the duration of the microwave hydrothermal treatment in minutes.

According to powder X-ray diffraction (XRD) analysis, all the precursors crystallize in the trigonal $\beta\text{-Ni}(\text{OH})_2$ crystal structure (sp.gr. $P\bar{3}m1$) with similar unit cell parameters ($a = 3.130(1)$ Å, $c = 4.617(1)$ Å for the MW_30m sample). No admixture peaks were observed (Figure 2 and Figure S3). According to STEM-EDX analysis, all precursors possess homogeneous distribution of Ni, Mn, and Co (Figure 3 and Figure S4) and the desired TM cation ratio (Table S1). To sum up, a combination of powder XRD (Figure 2 and Figure S3) and STEM-EDX (Figure 3 and Figure S4) data indicates that variation of the hydrothermal treatment time does not impact phase purity, composition and TM distribution of the obtained precursors. Contrarily, the morphology of the precursors clearly depends on the microwave hydrothermal treatment duration (Figure 4). The mixed hydroxides consist of flower-shaped agglomerates of flake-like primary particles. Enhancement of the hydrothermal treatment time increases the average size of the primary particles from 400 nm to 600 nm and 800 nm for the MW_15m, MW_30m, and MW_60m samples, respectively.

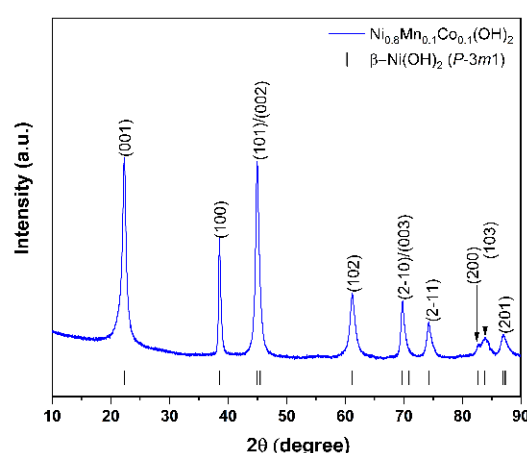


Figure 2. Powder XRD pattern (blue curve) of the MW_30m $\text{Ni}_{0.8}\text{Mn}_{0.1}\text{Co}_{0.1}(\text{OH})_2$ precursor. Bragg reflection positions for the $\beta\text{-Ni}(\text{OH})_2$ structure are marked with black vertical lines.

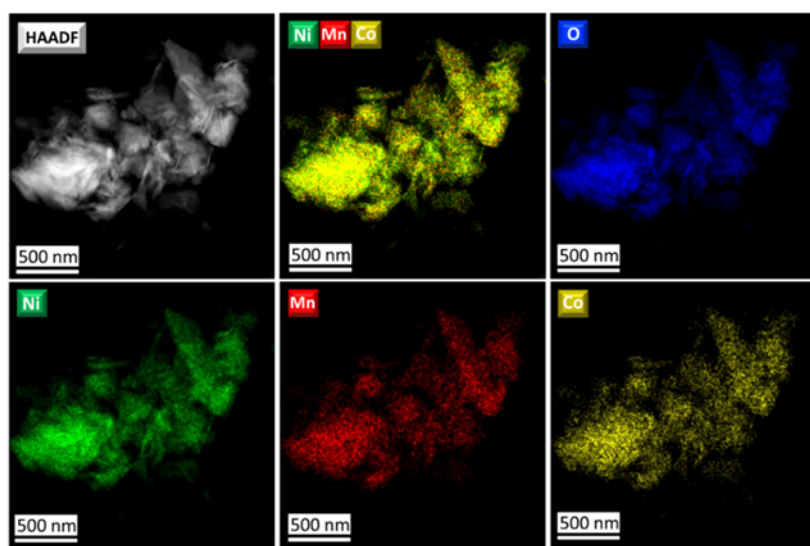


Figure 3. HAADF-STEM image of the MW_30m hydroxide precursor along with the corresponding color-coded STEM-EDX compositional map and elemental maps of O, Ni, Mn, and Co.

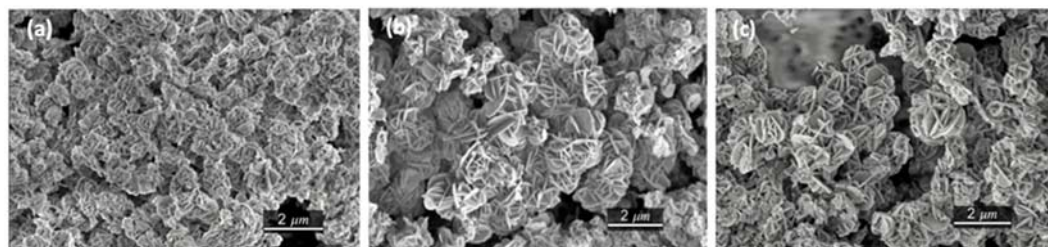


Figure 4. SEM images of the hydroxide precursors MW_15m (a), MW_30m (b), and MW_60m (c).

The obtained precursors were sintered with LiOH·H₂O in flowing oxygen to prepare the final NMC811 cathode materials MW_15m_A, MW_30m_A, and MW_60m_A. According to powder XRD data, all NMC811 samples are single-phase compounds crystallized in the layered α -NaFeO₂-type structure (sp. gr. $R\bar{3}m$). Moreover, a distinct splitting of the (006)/(012) and (108)/(110) peaks indicates a formation of the highly-ordered layered hexagonal structure (Figure 5 and Figure S5) [18]. The unit cell parameters and the degree of Ni²⁺/Li⁺ disorder, originated from partial exchange of the Li⁺ ($r_{\text{IV}} = 0.76 \text{ \AA}$) and Ni²⁺ ($r_{\text{IV}} = 0.69 \text{ \AA}$) cations between the 3b (i.e., Li) and 3a (i.e., Ni) sites were calculated for all samples using Rietveld refinement from powder XRD data (Table 1) [19]. The experimental, calculated and difference XRD patterns are shown in Figure 5. All the samples exhibit low cation disorder comparable for both microwave hydrothermal (MW) and co-precipitation (CP) synthesis techniques (Table 1). Similar values suggest that the synthetic route, as well as treatment time, negligibly impact the crystal structure of the final NMC811 materials.

Table 1. Crystallographic data after the Rietveld refinement for the LiNi_{0.8}Mn_{0.1}Co_{0.1}O₂ samples.

Sample	<i>a</i> , Å	<i>c</i> , Å	<i>V</i> , Å ³	Ni ²⁺ in 3a Site, %	Li ⁺ in 3b Site, %	R _I , R _P , wR _P , %
MW_15m_A	2.8729(8)	14.2087(1)	101.5666(7)	1.73(7)	3.88(6)	1.07, 2.23, 2.97
MW_30m_A	2.8706(3)	14.1979(1)	101.3232(7)	1.67(5)	3.97(8)	1.29, 2.03, 2.69
MW_60m_A	2.8732(1)	14.2084(1)	101.5801(6)	1.83(4)	3.15(1)	1.34, 2.15, 2.84
CP_A	2.8721(2)	14.2044(2)	101.4750(2)	2.54(4)	5.28(2)	1.73, 1.92, 2.62

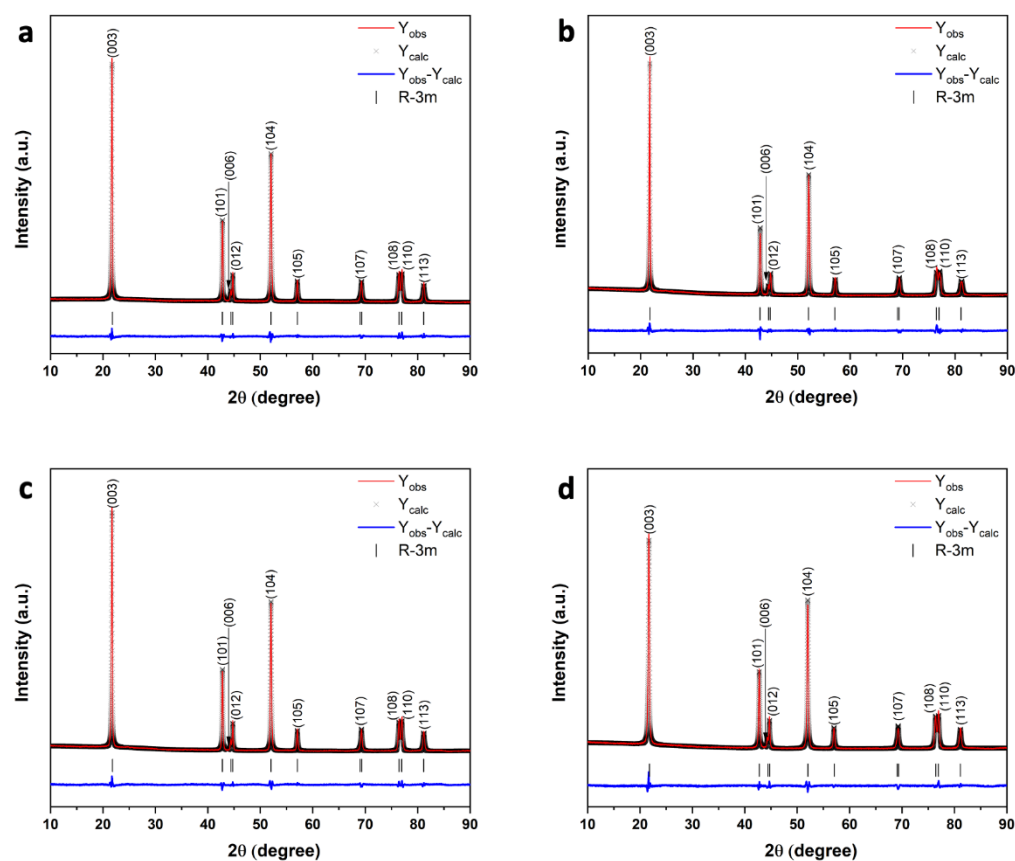


Figure 5. Experimental (black), calculated (red) and difference (blue) powder XRD patterns of the MW_15m_A (**a**), MW_30m_A (**b**), MW_60m_A (**c**) and CP_A (**d**) samples after Rietveld refinement. Bragg reflection positions (sp. gr. $R\bar{3}m$) are marked with black vertical lines.

According to STEM-EDX analysis, all NMC811 materials, regardless of the synthesis conditions, demonstrate uniform Ni, Mn, and Co distribution (Figure 6 and Figure S6). The Li content in all samples was measured by ICP-MS and the transition metal content was assessed by EDX analysis. The cationic composition in all samples is in good accordance with the desired stoichiometry (Table 2).

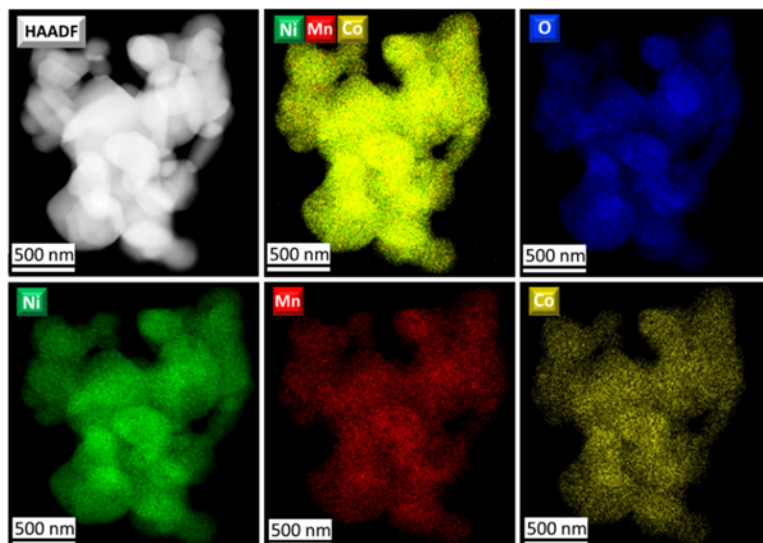


Figure 6. HAADF-STEM image of the MW_30m_A NMC811 sample along with the corresponding color-coded STEM-EDX compositional map and elemental maps of O, Ni, Mn, and Co.

Table 2. ICP-MS and EDX quantitative elemental analysis for the NMC811 samples obtained via different routes.

Sample	Li, mol. Fraction (ICP-MS)	Ni, mol. Fraction	Mn, mol. Fraction	Co, mol. Fraction
MW_15m_A	0.98 ± 0.06	0.812 ± 0.022	0.097 ± 0.010	0.091 ± 0.018
MW_30m_A	1.08 ± 0.04	0.804 ± 0.019	0.096 ± 0.005	0.100 ± 0.030
MW_60m_A	0.93 ± 0.08	0.815 ± 0.024	0.091 ± 0.008	0.094 ± 0.026
CP_A	1.02 ± 0.06	0.795 ± 0.024	0.106 ± 0.024	0.099 ± 0.024

Additionally, the local structure of the NMC811 samples was investigated by high-resolution HAADF-STEM imaging and selected area electron diffraction (SAED) (Figure 7). All reflections in the SAED patterns can be indexed in the rhombohedral $\bar{R}\bar{3}m$ structure with the unit cell parameters $a \approx 2.9 \text{ \AA}$, $c \approx 14.2 \text{ \AA}$, in good agreement with the powder XRD data (Table 1). The well-established layered structure can be recognized in the HAADF-STEM images as rows of bright dots corresponding to the TM atomic columns. The TM layers alternate along the c -axis with dark gaps, which are the Li layers. The O3 stacking sequence manifests itself as a lateral shift of every next TM layer over $1/3$ of the interdot distance. Slight HAADF intensity observed at the Li layers proves that Li/TM disordering is small, corroborating the Rietveld refinement results.

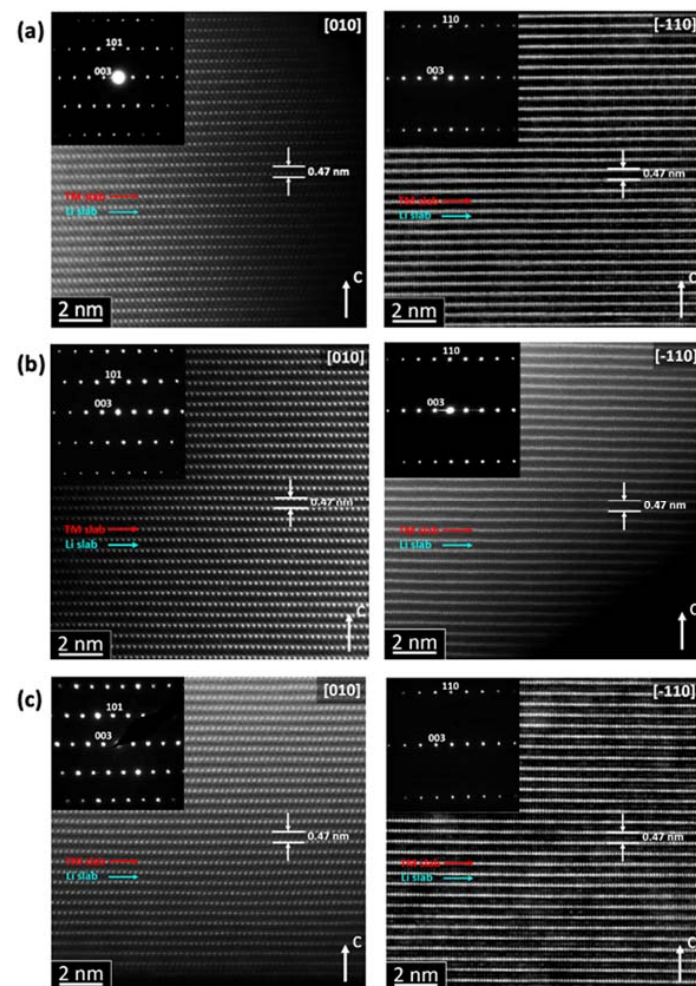


Figure 7. [010] and $[\bar{1}\bar{1}0]$ HAADF-STEM images along with the corresponding SAED patterns of MW_15m_A (a); MW_30m_A (b); MW_60m_A (c) NMC811 samples. Indexes in the SAED patterns correspond to the rhombohedral $\bar{R}\bar{3}m$ structure.

The annealed MW samples consist of irregularly-shaped agglomerates composed of primary particles (Figure 8) with an average size of 250, 400, and 500 nm for the MW_15m_A, MW_30m_A, and MW_60m_A samples, respectively (Figure S7). The increase of the primary particle size follows the particle size variation in the corresponding precursors.

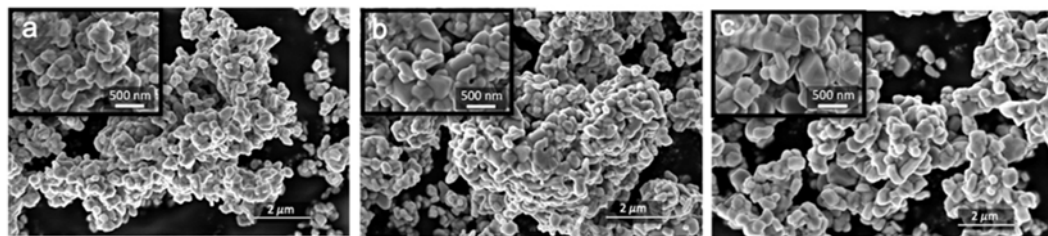


Figure 8. SEM images of the MW_15m_A (a), MW_30m_A (b) and MW_60m_A (c) NMC811 samples.

NMC811 material obtained via the conventional co-precipitation route (CP_A) is single-phase and crystallizes in the layered α -NaFeO₂ structure type (sp. gr. $R\bar{3}m$) (Figure 5) with a low degree of anti-site disordering (2.42(5)% of Ni²⁺ in 3a site). The homogeneous distribution of Ni, Mn, and Co and chemical composition were confirmed by STEM-EDX (Figure S8). The co-precipitated NMC811 sample is formed by roundish agglomerates with a size of ~8–12 μ m consisting of rectangular primary particles of 350 nm (Figure S9).

The electrochemical performance of the NMC811 materials was investigated using galvanostatic cycling, and their specific discharge capacity plots are given in Figure 9. The MW and CP samples demonstrate similar electrochemical performance (Table 3), still, the maximum discharge capacity of 203 mAh/g and maximum capacity retention of 73% after 300 charge/discharge cycles at 1C current density is achieved in the MW_30m_A sample.

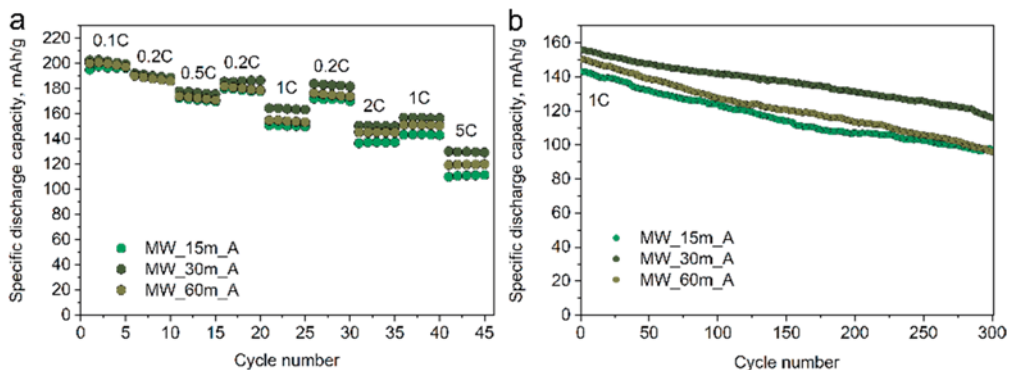


Figure 9. Rate capability (a) and cycling stability at 1C rate (b) of the MW NMC811 samples.

Table 3. Discharge capacity and capacity retention for the MW and CP NMC811 samples.

Sample	1st Cycle CE, %	Discharge Capacity, mAh/g					Capacity Retention, at 1C, %			
		0.1C	0.2C	0.5C	1C	2C	5C	after 100 Cycles	after 200 Cycles	after 300 Cycles
MW_15m_A	82	198	190	172	150	137	110	87	75	68
MW_30m_A	87	203	192	178	165	151	130	91	84	73
MW_60m_A	84	200	190	174	154	145	120	85	74	64
CP_A	78	199	192	178	165	156	131	90	77	69
CP7_MW3	83	202	194	182	165	144	120	93	85	78
NCM811 [20]	82	196	180	162	150	125	100	87	79	-

To evaluate the processes taking place during Li (de)intercalation in NMC811, differential capacity (dQ/dV) profiles were plotted for all the obtained materials (Figure S10). The NMC811 samples undergo a series of phase transitions during charge/discharge, as corroborated by the several oxidation peaks denoted in Figure S10: hexagonal-to-monoclinic

(H1 \rightarrow M), monoclinic-to-hexagonal (M \rightarrow H2) and hexagonal-to-hexagonal (H2 \rightarrow H3) [21]. The H2 \rightarrow H3 transformation at a high delithiation degree is believed to have the most substantial negative effect on the cycling stability of NMC811, as it is accompanied by anisotropic volume change that destabilizes the mechanical integrity of the cathode particles and accelerates capacity fading [22–27]. The intensity of the H2 \rightarrow H3 cathodic peak for the MW_60m_A material markedly dropped after 100 cycles at 1C (Figure S10c), indicating poor reversibility of the H2 \rightarrow H3 phase transformation considered as a source of severe structural collapse affected by mechanical strain [28]. Oppositely, other materials maintain the H2 \rightarrow H3 peaks over 100 cycles (Figure S10a,b), confirming the remarkable reversibility of the H2 \rightarrow H3 transition.

An additional comparative SEM study of the as-prepared and cycled 330 times electrodes (Figure 10 and Figure S11) was performed to reveal the influence of prolonged cycling on the microstructure of electrode materials. While the crystallites of the active material in MW_15m_A and MW_30m_A electrodes retain their integrity after cycling (Figure S11c,d), microcracks across the cathode primary particles are observed in the cycled MW_60m_A-based cathode (Figure 10b). The particle size distributions for MW_15m_A and MW_30m_A after cycling remain similar to those in the pristine materials, while for MW_60m_A the average particle size decreases dramatically from ~500 nm to around 250–300 nm (Figure S12) due to cracking upon multiple cycles. These detrimental effects are associated with mechanical stresses induced by repetitive volume expansion and contraction of the particles during electrochemical cycling. As seen in Figure S7, the broadest particle size distribution was observed for the MW_60m_A sample. It may result in uneven charging of particles of different sizes and finally promote the structural collapse of the biggest ones [29]. Hence, we considered the prolonged microwave treatment as not favorable for obtaining the particles with a sufficiently narrow size distribution that compromises the capacity retention.

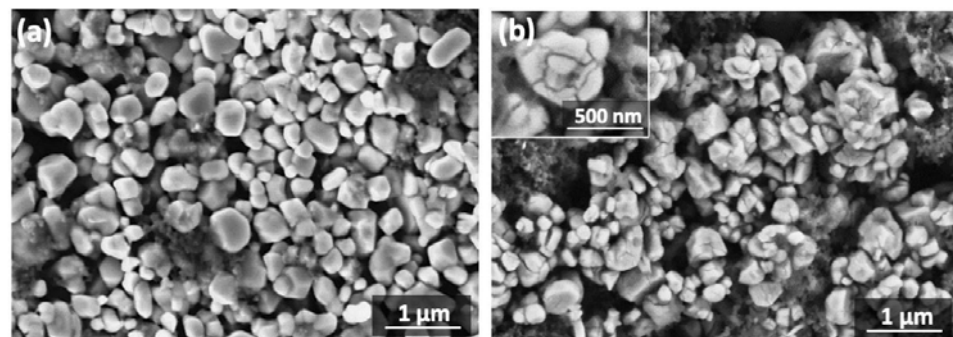


Figure 10. SEM images of the pristine (a) and cycled 330 times (b) MW_60m_A NMC811 electrodes. The magnified SEM image of the cracked particle after 330 cycles is provided in the inset.

The SEM images demonstrate that the NMC811 samples prepared via microwave-assisted hydrothermal route consist of poorly agglomerated particles of a several times smaller size than the agglomerates in the CP-prepared material. These observations were also supported by BET-specific surface areas for the MW_30m_A sample with the best electrochemical performance and for the co-precipitated reference material. Predictably, the specific surface area for MW_30m_A is higher than that for the CP_A sample (0.99 vs. 0.60 m^2/g , respectively). As a result, the as-prepared MW_30m_A material demonstrates a lower tap density of 1.7 g/cm^3 compared to the CP_A sample with a tap density of 2.3 g/cm^3 . On the one hand, it leads to lower volumetric energy density for MW_30m_A which calls for further development of annealing with sintering additives [30]. On the other hand, it has been reported previously for NMC532 [9] that tap density can be improved by mixing materials with different particle size distributions in an optimal mass ratio. Random packing of equal spheres achieved by the tapping method results in an average space filling of 64% [31]. Adding a fraction with a smaller particle size allows for filling

the voids between the spheres and, therefore, improves the tap density. Thus, to get the NMC811 material with the best tap density, we mixed the spherical agglomerates of the CP_A powder with the MW_30m_A sample consisting of small 200–700 nm crystallites. The optimal mass ratio between CP_A and MW_30m_A samples was found to be 7:3 (the sample is denoted as CP7_MW3), which raised the tap density of the resulting NMC811 by 30% to 2.9 g/cm^3 from 2.3 g/cm^3 for the pure CP_A powder (Figure 11). When the mass fraction of MW_30m_A exceeds 30%, the tap density starts to decrease because all the voids between CP_A spheres are filled, and now the space between the MW_30m_A particles contributes to enhancing the total unoccupied volume.

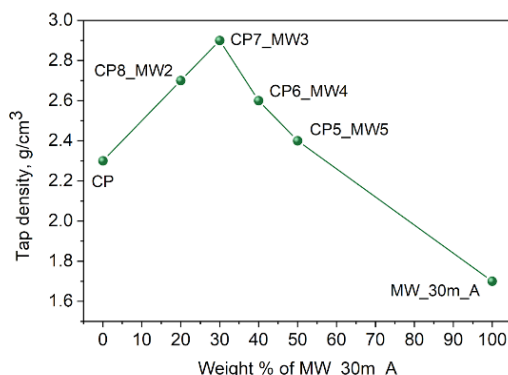


Figure 11. The tap density of NMC811 obtained by mixing the CP_A and MW_30m_A samples at various mass ratios (the line is a guide to the eye).

The electrochemical performance of the CP7_MW3 material was studied in both half- and full-cell configurations and compared to that of the CP_A sample. The mixed CP7_MW3 material demonstrates very similar to CP_A reversible discharge capacity at low current density but slightly lower capacity at high current density, i.e., 144 mAh/g and 120 mAh/g at 2C and 5C, respectively (Figure 12). In turn, capacity retention for CP7_MW3 of 85% and 78% after 200 and 300 cycles at 1C (Figure S13) noticeably exceeds the corresponding values of 77% and 69% for CP_A (Table 3) because of the addition of more electrochemically stable MW_30m_A particles giving a decent trade-off between the electrochemical cycling stability and tap density of the resulting cathode material. However, in full cells, the difference in capacity retention of the CP7_MW3 and CP_A samples becomes less pronounced. Both materials demonstrate capacity retention of 88–90% after 300 cycles at 1C (Figure 13). Nevertheless, due to increased tap density, the volumetric energy density was calculated to exceed 2100 mWh/cm³, while for the CP_A sample, it reached only 1690 mWh/cm³ (Table 4).

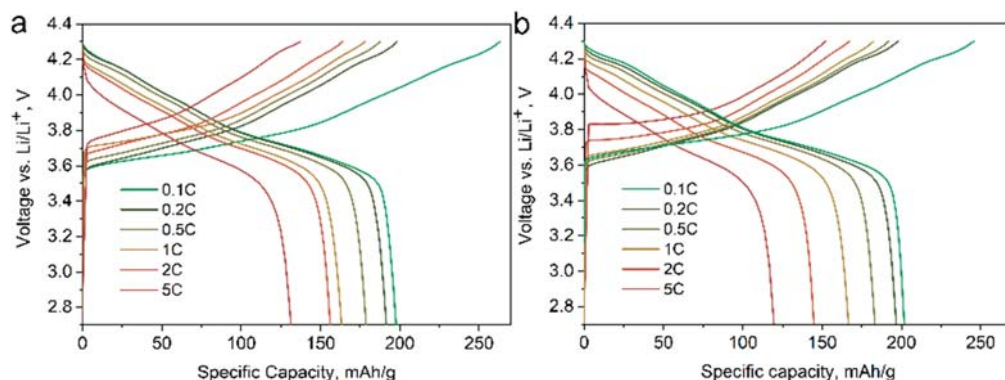


Figure 12. Galvanostatic charge-discharge curves at different current densities for the NMC811 samples CP_A (a) and CP7_MW3 (b) in half cells with metallic lithium anode.

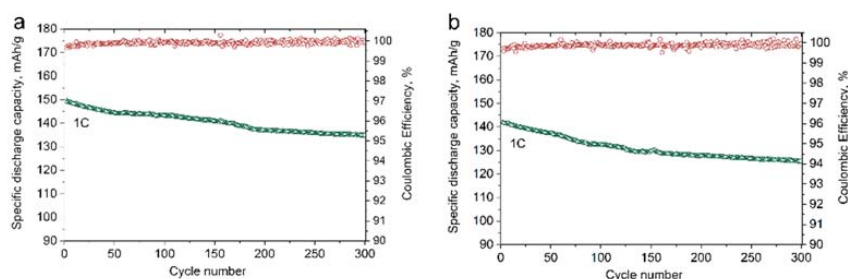


Figure 13. Capacity retention (green circles) and Coulombic efficiency (red circles) at 1C rate for the NMC811 samples CP_A (**a**) and CP7_MW3 (**b**) in full cells with the LTO anode.

Table 4. Comparison of tap densities and basic electrochemical characteristics of the initial MW, CP, and mixed samples.

Sample	Tap Density, g/cm ³	Discharge Capacity at 0.1 C, mAh/g	Volumetric Energy Density, mWh/cm ³
CP_A	2.3	199	1693
MW_30m_A	1.7	203	1277
CP7_MW3	2.9	202	2167

To obtain a deeper insight into the electrochemical performance of prepared NMCs, electrochemical impedance spectroscopy (EIS) study has been carried out. The typical Nyquist plot for Li battery with Ni-rich NMC cathode material includes contributions from the electrolyte solution resistance (R_{sol}), interface resistance and capacitance (R_{SEI} and C_{SEI}), charge transfer resistance (R_{ct}), double layer capacitance (C_{dl}) and diffusion elements. The Nyquist plots of the CP7_MW3, MW_30m_A, and CP_A materials charged up to 3.7 V are presented in Figure 14. All spectra include two semicircles in high- and low-frequency regions. High surface resistances are observed for the mixed CP7_MW3 (34.33 Ω) and microwave-prepared MW_30m_A (29.49 Ω) samples, while co-precipitation provides the material CP_A with the smallest R_{SEI} (14.22 Ω) indicating thinner passivation film accumulated on the electrode surface. This is in good agreement with the morphology of the CP7_MW3 and MW_30m_A samples: non-agglomerated particles, having higher surface area, are expected to increase interfacial resistance due to the increased number of contacts between the particles. At the same time, the CP_A sample demonstrates the highest charge transfer resistance R_{ct} (85.82 Ω), whereas CP7_MW3 and MW_30m_A are characterized by R_{ct} of 67.89 Ω and 48.18 Ω , respectively. In this sense, the trade-off between R_{ct} and R_{SEI} results (Table S2) in similar rate performance of CP7_MW3, MW_30m_A, and CP_A samples.

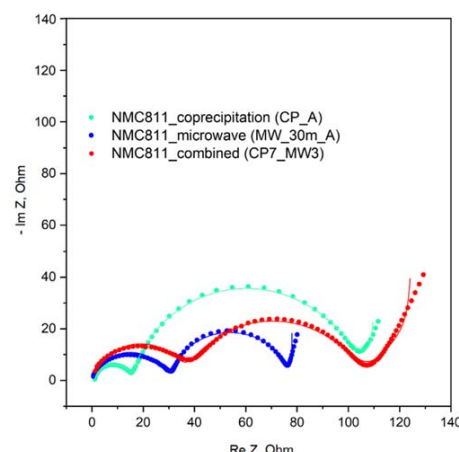


Figure 14. Nyquist plots and equivalent circuit fit (see Table S2 of Supplementary Materials for the fit parameters) for the NMC811 samples prepared via microwave-assisted hydrothermal and co-precipitation techniques, and the mix of these two samples.

3. Materials and Methods

Stoichiometric amounts (Ni:Mn:Co = 8:1:1) of $\text{NiSO}_4 \cdot 6\text{H}_2\text{O}$, $\text{MnSO}_4 \cdot \text{H}_2\text{O}$, $\text{CoSO}_4 \cdot 7\text{H}_2\text{O}$ (Alfa Aesar, $\geq 99\%$) were dissolved in 30 mL of deionized water with the resulting TM solution concentration of 0.20 mol/L. Glycine (Ruskhim) as a complexing agent was added to the TM solution with TM:Gly = 1:13.35 molar ratio, and the solution was stirred at room temperature for 10–20 min to obtain a transparent green solution (designated as Solution 1 in Figure 1), corresponding to the water-soluble TM complexes with glycine. Afterwards, the preliminary prepared 10 mL of 15 mol/L solution of NaOH (Ruskhim, $\geq 99.9\%$) as a precipitating agent (Solution 2 in Figure 1) was added dropwise into Solution 1 under magnetic stirring. Finally, a slurry-like blue precipitate of hydrates of disodium bis-glycylglycine complexes of TMs [32] was formed. The synthesis of the $\text{Ni}_{0.8}\text{Mn}_{0.1}\text{Co}_{0.1}(\text{OH})_2$ precursor via microwave-assisted hydrothermal technique was conducted using a WX-8000 Microwave Digestion System. For this, a suspension was transferred into an 80 mL Teflon vessel with 50% loading and treated under microwave hydrothermal conditions at 160 °C for 15, 30, and 60 min. The pressure inside the vessel was held at about 6 bar. Then the reactor was cooled to room temperature. The obtained precursors are labeled as MW_15m, MW_30m, and MW_60m. Upscaling of the microwave-assisted hydrothermal synthesis was conducted using the same microwave system and keeping the ratios of the starting reagents and their concentrations, but increasing the number of vessels to 10. The total slurry volume which was treated simultaneously under microwave conditions equals 400 mL. This resulted in a routine preparation of 10 g batches of the single-phase $\text{Ni}_{0.8}\text{Mn}_{0.1}\text{Co}_{0.1}(\text{OH})_2$ precursor.

The $\text{Ni}_{0.8}\text{Mn}_{0.1}\text{Co}_{0.1}(\text{OH})_2$ precursor was also synthesized via a conventional co-precipitation method. An aqueous solution of TM sulfates with the molar ratio of Ni:Mn:Co = 8:1:1 and a total concentration of 2 mol/L ($V_1 = 1\text{ L}$) was slowly pumped into a 5 L continuously stirred batch reactor, which was pre-filled with a certain amount of deionized water and $\text{NH}_3 \cdot \text{H}_2\text{O}$ solution under Ar atmosphere. Simultaneously, an aqueous solution of 4 mol/L ($V_2 = 300\text{ mL}$) NaOH and 4 mol/L $\text{NH}_3 \cdot \text{H}_2\text{O}$ were separately pumped into the reactor at a feeding rate of about 5 mL/min as the precipitating and complexing agents, respectively. The continuous stirring was kept at 800 rpm. The reactor temperature was maintained at 50 °C, and pH was fixed to 11.5. After co-precipitation, the resulting reaction mixture was kept at 50 °C under stirring for about 24 h for aging. The co-precipitated sample is designated as CP.

The greenish precursors, obtained with microwave-assisted hydrothermal synthesis and co-precipitation technique, were centrifuged, washed with distilled water several times, and dried at 90 °C for ~ 12 h under dynamic vacuum. The precursors were then mixed with $\text{LiOH} \cdot \text{H}_2\text{O}$ (Ruskhim) in a molar ratio of 1:1.05, and annealed at 750 °C for 12 h in flowing oxygen to prepare the final $\text{LiNi}_{0.8}\text{Mn}_{0.1}\text{Co}_{0.1}\text{O}_2$ (NMC811). The lithiated samples are designated as MW_15m_A, MW_30m_A, MW_60m_A, and CP_A. Mixed materials are designated as CP5_MW5, CP6_MW4, CP7_MW3, and CP8_MW2 where the numbers correspond to the mass ratio of CP_A and MW_30m_A samples.

Powder X-ray diffraction (XRD) data were collected using a Huber G670 Guinier diffractometer ($\text{CoK}_{\alpha 1}$ radiation ($\lambda = 1.78892\text{ \AA}$), curved Ge (111) monochromator, image plate detector). The patterns were measured at ambient temperature with a step of 0.005° within the 4–100° 2θ range and then were fitted through Le Bail and Rietveld methods. The program package JANA2006 [33] was used for data processing.

Particle morphology and size distribution in the pristine and cycled electrodes were investigated by scanning electron microscopy (SEM) using a ThermoFisher Quattro S microscope.

Selected area electron diffraction (SAED) patterns, high angle annular dark-field scanning transmission electron microscopy (HAADF-STEM) images, and energy-dispersive X-ray spectra in a STEM mode (STEM-EDX) were acquired using an aberration-corrected ThermoFisher Titan Themis Z transmission electron microscope operating at 200 kV and equipped with a Super-X system for EDX analysis. The samples were prepared in the air by crushing the powders with an agate mortar and pestle in ethanol and dropping the suspension onto a carbon film supported by a copper grid.

Nitrogen adsorption analysis of specific surface area was performed with a Quantachrome Instruments NOVA 2000 high-speed surface area analyzer at 77 K. Prior to the measurements, the samples were degassed in a dynamic vacuum for at least 12 h at 300 °C. The specific surface area was calculated using the Brunauer–Emmett–Teller (BET) method from the nitrogen adsorption data in the relative pressure range (P/P_0) from 0.045 to 0.233.

The tap density of the materials was determined with a tap density analyzer Quantachrome Autotap. At least 20 g of powder was poured into a 50 mL glass cylinder, and the cylinder was tapped 3000 times before measuring the sample volume.

The total Li content in the NMC811 samples was determined by mass-spectrometry with inductively coupled plasma (ICP-MS) using a Perkin-Elmer ELAN DRC-II mass-spectrometer. Aqueous solutions for the analysis were prepared by dissolving ~17.5 mg of the NMC811 powders in 1–2 mL of concentrated HNO₃ and HCl (1:3 vol. ratio) with subsequent dilution to 250 mL with deionized water. The standard calibration solutions were prepared by dissolving corresponding amounts of Li₂SO₄ (Sigma-Aldrich, 99.99%) in deionized water to obtain solutions with concentrations ranging from 2.0 mg/L to 10.0 mg/L.

In order to investigate the electrochemical properties, the NMC811 samples (80 wt.%) were mixed with carbon (Super-P) as a conductive phase (10 wt.%), polyvinylidene fluoride (PVdF) (10 wt.%) as a binder, and N-methyl-2-pyrrolidone (NMP) as a solvent. The active mass loading varies in a range of $2.55 \pm 0.2 \text{ mg/cm}^2$. The resulting homogeneous slurry was tape-casted onto a carbon-coated Al current collector using an automatic film applicator Zehntner ZAA 2300, dried at 70 °C, and then cut into disks with a diameter of 16 mm. Coin-type half-cells (2032 R) were assembled in an Ar-filled glove box using the electrolyte consisting of 1M LiPF₆ (Sigma-Aldrich, 99.99%) solution in ethylene carbonate/propylene carbonate/dimethyl carbonate solution (EC:PC:DMC = 1:1:3 vol. ratio). Galvanostatic tests were performed using a Neware BTS4000-5V10mA Battery Testing System with a lithium foil disc as a counter electrode in the potential range of 2.7–4.3 V at room temperature at different current rates from 0.1C to 5C (1C = 200 mA/g).

Full cells were assembled with the synthesized cathode materials and commercially available Li₄Ti₅O₁₂ (LTO) as the anode. Cathodes for full cells were prepared similarly to the cathodes for half-cells with the mass loading of 2.4–3.6 mg/cm². The active LTO anode material (TOB), conductive additive (Super-P), and PVdF binder were suspended in NMP with a weight ratio of 92:3:5 and homogenized to form a slurry. This slurry was applied onto a carbon-coated aluminum current collector using an automatic film applicator Zehntner ZAA 2300, dried, and then cut into 15 mm diameter disks with cathode loading of 3.7–4.4 mg/cm². 1 M LiPF₆ solution in ethylene carbonate/ethyl methyl carbonate solution (EC:EMC = 2:5 by weight) + 2 wt.% of vinylene carbonate was used as an electrolyte. A 3-layer polyethylene/polypropylene/polyethylene (PP/PE/PP) Celgard 2325 polymer film with a thickness of 25 µm was used as a separator. The full cells were assembled in an Ar-filled glove box and rested for 12 h at room temperature to ensure sufficient wetting. As a formation procedure, charging and discharging in a galvanostatic mode at 0.1C, 0.3C, 0.5C, and 1C (3 times) were performed in the potential range of 1.60–2.65 V at room temperature. Capacity retention tests were performed after formation in the same potential range at 1C in the constant current (CC)—constant voltage (CV) charge regime (charge with 1C constant current till 2.65 V with the subsequent charge at the constant voltage at 2.65 V (corresponds to ~4.25 V vs. Li/Li⁺) till 0.05 C current density) and CC discharge (1C constant current till 1.60 V) at room temperature. Electrochemical impedance spectroscopy (EIS) measurements were performed in a three-electrode cell configuration with lithium metal as a counter and reference electrode. Tests were conducted using a Biologic VMP3 potentiostat in the frequency range from 100 kHz to 10 mHz with the amplitude of AC signal of 5 mV at 3.7 V.

4. Conclusions

The microwave-assisted hydrothermal synthesis of a precursor for the LiNi_{0.8}Mn_{0.1}Co_{0.1}O₂ (NMC811) cathode for Li-ion battery was developed, shortening the reaction time from dozens of hours in a conventional co-precipitation method to dozens of minutes. The

microwave-assisted hydrothermal route provides a well-crystallized material with a relatively low degree of Li/TM disordering and homogeneous elemental distribution. The obtained NMC811 materials demonstrate a reversible capacity up to ~200 mAh/g at 0.1C current density and remarkable cycling stability in both half-cell and full-cell configurations. At the same time, small particles (200–700 nm) of the microwave-assisted hydrothermally prepared material can serve as excellent space-fillers to fill the voids between spherical agglomerates in NMC811 powder prepared through co-precipitation. Mixing them with the co-precipitated sample in a mass ratio of 3:7 increases the tap density by 30% from 2.3 to 2.9 g/cm³, boosting the volumetric energy density of NMC811 from 1690 mWh/cm³ to more than 2100 mWh/cm³. The suggested approach can be appointed as another step toward the energy-saving production of new-generation cathode materials for high energy density LIBs.

Supplementary Materials: The following supporting information can be downloaded at: <https://www.mdpi.com/article/10.3390/batteries8070067/s1>, Figure S1: Typical HAADF-STEM images of the Ni_{0.8}Mn_{0.1}Co_{0.1}(OH)₂ precursor obtained via microwave-assisted hydrothermal route with low glycine concentration along with color-coded STEM-EDX compositional map and elemental maps of O, Ni, Mn, and Co; Figure S2: SEM image of Ni_{0.8}Mn_{0.1}Co_{0.1}(OH)₂ sample obtained using microwave-assisted hydrothermal route with low NaOH concentration; Figure S3: Powder XRD patterns for the Ni_{0.8}Mn_{0.1}Co_{0.1}(OH)₂ precursors MW_15m (a), MW_60m (b) and CP (c); Figure S4: HAADF-STEM images of the MW_15m (a) and MW_60m (b) hydroxide precursors along with the corresponding color-coded STEM-EDX compositional maps and elemental maps of O, Ni, Mn, and Co; Figure S5: Splitting of (006)/(012) and (108)/(110) peaks on experimental (black), calculated (red) and difference (blue) powder XRD patterns of the MW_15m_A (a), MW_30m_A (b), MW_60m_A (c) and CP_A (d) samples after Rietveld refinement; Figure S6: HAADF-STEM images of the MW_15m_A (a) and MW_60m_A (b) NMC811 samples along with the corresponding color-coded STEM-EDX compositional maps and elemental maps of O, Ni, Mn, and Co; Figure S7: Size distributions of the primary particles in the NMC811 samples MW_15m_A (a), MW_30m_A (b) and MW_60m_A (c); Figure S8: HAADF-STEM image of the CP_A NMC811 sample obtained through co-precipitation route along with the color-coded STEM-EDX compositional map and elemental maps of O, Ni, Mn, and Co; Figure S9: SEM images of the CP_A NMC811 sample obtained through co-precipitation; Figure S10: Differential capacity plots for the NMC811 MW_15m_A (a), MW_30m_A (b) and MW_60m_A (c) samples; Figure S11: SEM images of the pristine (a,b) and 330 times cycled (c, d) NMC811 electrodes of the MW_15m_A (a,c) and MW_30m_A (b, d) samples; Figure S12: Size distributions of the primary particles in the NMC811 electrodes MW_15m_A (a), MW_30m_A (b) and MW_60m_A (c) after 330 charge/discharge cycles; Figure S13: Capacity retention at 1C rate of the CP_A and CP7_MW3 NMC811 samples in half-cells with metallic lithium anode; Table S1: Quantitative EDX analysis for the Ni_{0.8}Mn_{0.1}Co_{0.1}(OH)₂ precursors. Table S2: The results of EIS approximation by selected equivalent circuit.

Author Contributions: Conceptualization, A.M.A. and A.A.S.; methodology, A.A.S.; validation, A.A.S.; formal analysis, I.S., E.D.O. and V.S.G.; investigation, I.S., E.D.O. and V.S.G.; resources, A.M.A.; data curation, A.M.A. and A.A.S.; writing—original draft preparation, I.S.; writing—review and editing, A.A.S. and A.M.A.; visualization, E.D.O.; supervision, A.M.A.; project administration, A.M.A.; funding acquisition, A.M.A. All authors have read and agreed to the published version of the manuscript.

Funding: This research was funded by the Russian Science Foundation grant number 20-13-00233.

Institutional Review Board Statement: Not applicable.

Informed Consent Statement: Not applicable.

Data Availability Statement: Not applicable.

Acknowledgments: The authors are grateful to Advanced Imaging Core Facility (AICF) of Skoltech for providing access to the Transmission Electron Microscopy (TEM) facilities. The authors acknowledge Russian Science Foundation (grant 20-13-00233).

Conflicts of Interest: The authors declare no conflict of interest.

References

- Myung, S.-T.; Maglia, F.; Park, K.-J.; Yoon, C.S.; Lamp, P.; Kim, S.-J.; Sun, Y.-K. Nickel-rich layered cathode materials for Automotive lithium-ion batteries: Achievements and perspectives. *ACS Energy Lett.* **2017**, *2*, 196–223. [[CrossRef](#)]
- Li, W.; Erickson, E.M.; Manthiram, A. High-nickel layered oxide cathodes for lithium-based automotive batteries. *Nat. Energy* **2020**, *5*, 26–34. [[CrossRef](#)]
- Cabelguen, P.-E.; Peralta, D.; Cugnet, M.; Maillet, P. Impact of morphological changes of $\text{LiNi}_{1/3}\text{Mn}_{1/3}\text{Co}_{1/3}\text{O}_2$ on lithium-ion cathode performances. *J. Power Sources* **2017**, *346*, 13–23. [[CrossRef](#)]
- Xu, G.-L.; Liu, X.; Daali, A.; Amine, R.; Chen, Z.; Amine, K. Challenges and strategies to advance high-energy nickel-rich layered lithium transition metal oxide cathodes for harsh operation. *Adv. Funct. Mater.* **2020**, *30*, 2004748. [[CrossRef](#)]
- Xia, Y.; Zheng, J.; Wang, C.; Gu, M. Designing principle for Ni-rich cathode materials with high energy density for practical applications. *Nano Energy* **2018**, *49*, 434–452. [[CrossRef](#)]
- He, P.; Wang, H.; Qi, L.; Osaka, T. Electrochemical characteristics of layered $\text{LiNi}_{1/3}\text{Co}_{1/3}\text{Mn}_{1/3}\text{O}_2$ and with different synthesis conditions. *J. Power Sources* **2006**, *160*, 627–632. [[CrossRef](#)]
- Zhao, Z.; Sun, M.; Wu, T.; Zhang, J.; Wang, P.; Zhang, L.; Yang, C.; Peng, C.; Lu, H. A bifunctional-modulated conformal Li/Mn-rich layered cathode for fast-charging, high volumetric density and durable Li-ion full cells. *Nano-Micro Lett.* **2021**, *13*, 118. [[CrossRef](#)]
- Yang, S.; Wang, X.; Yang, X.; Liu, Z.; Wei, Q.; Shu, H. High tap density spherical $\text{Li}[\text{Ni}_{0.5}\text{Mn}_{0.3}\text{Co}_{0.2}]\text{O}_2$ cathode material synthesized via continuous hydroxide coprecipitation method for advanced lithium-ion batteries. *Int. J. Electrochem.* **2012**, *2012*, 323560. [[CrossRef](#)]
- Zhang, Y.; Wang, Z.B.; Nie, M.; Yu, F.D.; Xia, Y.F.; Liu, B.S.; Xue, Y.; Zheng, L.L.; Wu, J. A simple method for industrialization to enhance the tap density of $\text{LiNi}_{0.5}\text{Co}_{0.2}\text{Mn}_{0.3}\text{O}_2$ cathode material for high-specific volumetric energy lithium-ion batteries. *RSC Adv.* **2016**, *6*, 65941–65949. [[CrossRef](#)]
- Yang, G.; Park, S.J. Conventional and microwave hydrothermal synthesis and application of functional materials: A review. *Materials* **2019**, *12*, 1177. [[CrossRef](#)]
- Komarneni, S.; Roy, R.; Li, Q.H. Microwave-hydrothermal synthesis of ceramic powders. *Mater. Res. Bull.* **1992**, *27*, 1393–1405. [[CrossRef](#)]
- Murugan, A.V.; Muraliganth, T.; Manthiram, A. Comparison of microwave assisted solvothermal and hydrothermal syntheses of LiFePO_4/C nanocomposite cathodes for lithium ion batteries. *J. Phys. Chem. C* **2008**, *112*, 14665–14671. [[CrossRef](#)]
- Burova, D.; Shakhova, I.; Morozova, P.; Iarchuk, A.; Drozhzhin, O.A.; Rozova, M.G.; Praneetha, S.; Murugan, V.; Tarascon, J.M.; Abakumov, A.M. The rapid microwave-assisted hydrothermal synthesis of NASICON-structured $\text{Na}_3\text{V}_2\text{O}_2\text{X}(\text{PO}_4)_2\text{F}_{3-2x}$ ($0 < x \leq 1$) cathode materials for Na-ion batteries. *RSC Adv.* **2019**, *9*, 19429–19440. [[CrossRef](#)] [[PubMed](#)]
- Wang, Y.; Zhu, Q. Electrochemical properties and controlled-synthesis of hierarchical $\beta\text{-Ni(OH)}_2$ micro-flowers and hollow microspheres. *Mater. Res. Bull.* **2010**, *45*, 1844–1849. [[CrossRef](#)]
- Mondal, A.K.; Su, D.; Chen, S.; Zhang, J.; Ung, A.; Wang, G. Microwave-assisted synthesis of spherical $\beta\text{-Ni(OH)}_2$ superstructures for electrochemical capacitors with excellent cycling stability. *Chem. Phys. Lett.* **2014**, *610–611*, 115–120. [[CrossRef](#)]
- Wang, Y.; Zhu, Q.; Zhang, H. Fabrication of $\beta\text{-Ni(OH)}_2$ and NiO hollow spheres by a facile template-free process. *Chem. Commun.* **2005**, *41*, 5231–5233. [[CrossRef](#)]
- Yang, X.; Wang, X.; Ching, C.B. Solubility of form α and form γ of glycine in aqueous solutions. *J. Chem. Eng. Data* **2008**, *53*, 1133–1137. [[CrossRef](#)]
- Thackeray, M.M.; Kang, S.H.; Johnson, C.S.; Vaughey, J.T.; Hackney, S.A. Comments on the structural complexity of lithium-rich $\text{Li}_{1+x}\text{M}_{1-x}\text{O}_2$ electrodes ($\text{M} = \text{Mn, Ni, Co}$) for lithium batteries. *Electrochem. Commun.* **2006**, *8*, 1531–1538. [[CrossRef](#)]
- Orlova, E.D.; Savina, A.A.; Abakumov, S.A.; Morozov, A.V.; Abakumov, A.M. Comprehensive study of $\text{Li}^+/\text{Ni}^{2+}$ disorder in Ni-rich NMCs cathodes for Li-ion batteries. *Symmetry* **2021**, *13*, 1628. [[CrossRef](#)]
- Dai, S.; Yan, G.; Wang, L.; Luo, L.; Li, Y.; Yang, Y.; Liu, H.; Liu, Y.; Yuan, M. Enhanced electrochemical performance and thermal properties of Ni-rich $\text{LiNi}_{0.8}\text{Co}_{0.1}\text{Mn}_{0.1}\text{O}_2$ cathode material via CaF_2 coating. *J. Electroanal. Chem.* **2019**, *847*, 113197. [[CrossRef](#)]
- Jung, R.; Metzger, M.; Maglia, F.; Stinner, C.; Gasteiger, H.A. Oxygen release and its effect on the cycling stability of $\text{LiNi}_x\text{Mn}_y\text{Co}_z\text{O}_2$ (NMC) cathode materials for Li-ion batteries. *J. Electrochem. Soc.* **2017**, *164*, A1361–A1377. [[CrossRef](#)]
- Zheng, S.; Hong, C.; Guan, X.; Xiang, Y.; Liu, X.; Xu, G.L.; Liu, R.; Zhong, G.; Zheng, F.; Li, Y.; et al. Correlation between long range and local structural changes in Ni-rich layered materials during charge and discharge process. *J. Power Sources* **2019**, *412*, 336–343. [[CrossRef](#)]
- Kim, J.H.; Ryu, H.H.; Kim, S.J.; Yoon, C.S.; Sun, Y.K. Degradation mechanism of highly Ni-rich $\text{Li}[\text{Ni}_x\text{Co}_y\text{Mn}_{1-x-y}]\text{O}_2$ cathodes with $x > 0.9$. *ACS Appl. Mater. Interfaces* **2019**, *11*, 30936–30942. [[CrossRef](#)]
- Li, J.; Downie, L.E.; Ma, L.; Qiu, W.; Dahn, J.R. Study of the failure mechanisms of $\text{LiNi}_{0.8}\text{Mn}_{0.1}\text{Co}_{0.1}\text{O}_2$ cathode material for lithium ion batteries. *J. Electrochem. Soc.* **2015**, *162*, A1401–A1408. [[CrossRef](#)]
- Ryu, H.H.; Park, K.J.; Yoon, C.S.; Sun, Y.K. Capacity fading of Ni-rich $\text{Li}[\text{Ni}_x\text{Co}_y\text{Mn}_{1-x-y}]\text{O}_2$ ($0.6 \leq x \leq 0.95$) cathodes for high-energy-density lithium-ion batteries: Bulk or surface degradation? *Chem. Mater.* **2018**, *30*, 1155–1163. [[CrossRef](#)]
- Yoon, C.S.; Ryu, H.H.; Park, G.T.; Kim, J.H.; Kim, K.H.; Sun, Y.K. Extracting maximum capacity from Ni-rich $\text{Li}[\text{Ni}_{0.95}\text{Co}_{0.025}\text{Mn}_{0.025}]\text{O}_2$ cathodes for high-energy-density lithium-ion batteries. *J. Mater. Chem. A* **2018**, *6*, 4126–4132. [[CrossRef](#)]
- Yoon, C.S.; Jun, D.W.; Myung, S.T.; Sun, Y.K. Structural stability of LiNiO_2 cycled above 4.2 V. *ACS Energy Lett.* **2017**, *2*, 1150–1155. [[CrossRef](#)]

28. Park, K.J.; Choi, M.J.; Maglia, F.; Kim, S.J.; Kim, K.H.; Yoon, C.S.; Sun, Y.K. High-capacity concentration gradient Li[Ni_{0.865}Co_{0.120}Al_{0.015}]O₂ cathode for lithium-ion batteries. *Adv. Energy Mater.* **2018**, *8*, 1703612. [[CrossRef](#)]
29. Hietaniemi, M.; Hu, T.; Välikangas, J.; Niittykoski, J.; Lassi, U. Effect of precursor particle size and morphology on lithiation of Ni_{0.6}Mn_{0.2}Co_{0.2}(OH)₂. *J. Appl. Electrochem.* **2021**, *51*, 1545–1557. [[CrossRef](#)]
30. Jouanneau, S.; Dahn, J.R. Influence of LiF additions on Li[Ni_xCo_{1–2x}Mn_x]O₂ materials. *J. Electrochem. Soc.* **2004**, *151*, A1749. [[CrossRef](#)]
31. Delaney, G.W.; Hilton, J.E.; Cleary, P.W. Defining random loose packing for nonspherical grains. *Phys. Rev. E* **2011**, *83*, 051305. [[CrossRef](#)] [[PubMed](#)]
32. Freeman, H.C.; Guss, J.M.; Sinclair, R.L. Crystal structures of four nickel complexes of glycine and glycine peptides. *Chem. Commun.* **1968**, *9*, 485–487. [[CrossRef](#)]
33. Petříček, V.; Dušek, M.; Palatinus, L. Crystallographic computing system JANA2006: General features. *Zeitschrift fur Kristallographie* **2014**, *229*, 345–352. [[CrossRef](#)]